The Astrophysical Journal, 593:534–548, 2003 August 10
© 2003. The American Astronomical Society. All rights reserved. Printed in U.S.A.

AN ESTIMATE OF THE SUN'S *ROSAT*-PSPC X-RAY LUMINOSITIES USING *SNOE*-SXP MEASUREMENTS

Philip G. Judge and Stanley C. Solomon
High Altitude Observatory, National Center for Atmospheric Research,[1] P.O. Box 3000, Boulder, CO 80307-3000

and

Thomas R. Ayres
CASA, 389-UCB, University of Colorado, Boulder, CO 80309-0389
Received 2002 December 4; accepted 2003 April 18

ABSTRACT

Using solar soft X-ray irradiance measurements from the SXP instrument on the *SNOE* satellite, we relate the solar surface flux densities and their variability to those of stars as measured with the PSPC instrument on *ROSAT*. We translate *SNOE*-SXP measurements into equivalent *ROSAT*-PSPC counts using model spectra calculated from the CHIANTI package. Using the *SNOE*-SXP measurements has significant advantages over earlier studies: the absolute calibration is known to ±25%, *SNOE* measures the Sun as if it were an unresolved star, it has operated over a significant fraction of the solar cycle, and its three wavelength channels overlap substantially with that of the *ROSAT*-PSPC instrument. The predicted solar X-ray luminosities and surface flux densities are compared with measurements from the *ROSAT* database. We find that we can estimate the luminosity of the Sun as seen in the 0.1–2.4 keV ("RASS") passband of *ROSAT*-PSPC to within ±50%, not counting sources of systematic uncertainty mentioned in an appendix: the result lies between $10^{27.1}$ and $10^{27.75}$ ergs s^{-1} (measured in the existing data set, only partially covering a full solar cycle) and between $10^{26.8}$ and $10^{27.9}$ ergs s^{-1} (extrapolated to the full activity range of a typical solar cycle). The solar luminosities lie close to the median behavior found for a volume-limited ($d < 13$ pc) sample of G stars studied in 1997 by Schmitt, revealing the Sun to be a normal or slightly inactive G dwarf. A factor of 1.5 peak-to-peak variation in the RASS passband is predicted due simply to rotational modulations (i.e., those filtered to include periods $P < 81$ days). The ratio of maximum/minimum RASS luminosities from the magnetic activity cycle (filtered to include periods $P > 81$ days) are estimated to be 0.7–0.8 in $\log_{10} L_{\rm RASS}$, a ratio of 5 or 6. These variations are much smaller than both recent estimates of solar X-ray variability and the range of X-ray luminosities seen within Schmitt's sample. It is suggested that the reported absence of "solar-like" cyclic emission in stellar X-rays might partly arise because the Sun is less variable than assumed in some earlier work. Repeated *ROSAT* observations of α Cen A during 1995–1998 show X-ray behavior reminiscent of the Sun during activity minimum conditions.

Subject headings: stars: coronae — Sun: corona — Sun: X-rays, gamma rays

1. INTRODUCTION

The Sun remains the only star whose surface properties can be studied in any real detail. Placing the Sun it its proper context among the stars therefore is an important task, which in principle can yield unique information of importance to both solar and stellar astrophysics. This task is not as simple as it might sound, because different instruments almost always are used to measure solar and stellar properties. Furthermore, many solar instruments take advantage of the fact that the solar disk can be spatially resolved, so that "Sun-as-a-star" data have to be reconstructed from spatially resolved images. Also, the large solar fluxes present special challenges. For example, accurate photometry of the Sun relative to the stars even at visible wavelengths is a nontrivial task (e.g., Taylor 1984; Gray 1992; Gustafsson 1998).

These and other sources of uncertainty are mirrored in the diversity of solar X-ray luminosities reported in the literature. For example, between 1 and 300 Å (0.04–12.4 keV) the range of solar cyclic variability is currently quoted as 3×10^{25} to 10^{27} ergs s^{-1} by Hünsch, Schmitt, & Voges (1998) and Hünsch et al. (1999), citing Haisch & Schmitt (1996) and Acton (1996). Very similar values are derived from Acton's (1996) preliminary tabulation of *Yohkoh*-SXT X-ray indexes averaged over Carrington rotations, converted using Acton's Table 2 to a narrower "*ROSAT*-PSPC" passband from 3 to 124 Å (0.1–4.0 keV). Haisch & Schmitt (1996) note that these estimates, based on *Yohkoh*-SXT data and emission measure analyses, yield typical solar minimum values closer to 10^{26} than 3×10^{25} ergs s^{-1}. In contrast, in an effort to relate solar cyclic variations to *ROSAT*-PSPC data, Ayres (1997) compiled results from several suborbital rocket measurements and obtained solar luminosities from 6×10^{26} to 2×10^{27} ergs s^{-1} for a band between 6.2 and 62 Å (0.2–2.0 keV) in his Figure 7. These data—in particular, the large discrepancy in the value of the minimum solar luminosity—are revisited in § 4, together with other measurements.

X-rays are generated in the coronae of the Sun and solar-type stars by mechanisms yet to be understood but that certainly involve magnetic fields (e.g., Vaiana & Rosner 1978). Placing solar X-rays accurately in the context of stars can in principle tell us a great deal about magnetic activity, extending beyond what is possible by studying the Sun or stars separately. Here we relate solar coronal emissions to the stars using data from the Solar X-Ray Photometer (SXP) instrument on board the *Student Nitric Oxide*

[1] The National Center for Atmospheric Research is sponsored by the National Science Foundation.

Explorer (*SNOE*) satellite (Bailey et al. 2000) and archival data from the Position Sensitive Proportional Counter (PSPC) instrument on the *ROSAT* satellite. Our aim is to place the mean coronal activity level, and the rotational and cyclic variations, of the Sun firmly among the stellar database obtained by *ROSAT*-PSPC. Given this goal, our approach is to transform the *SNOE*-SXP measurements, which have no imaging capability, into *ROSAT*-PSPC count rates, taking advantage of the substantial overlap in wavelength coverage of the two different instruments. Our technique and results differ from some earlier work based on solar images from *Yohkoh*-SXT (e.g., Acton 1996; Orlando, Peres, & Reale 2001), which are sensitive to higher energy spectra, and these differences are explored in § 4. We first review relevant instrumental properties, then describe a simple method that relates the two data sets via simulations of the coronal thermal emission based on the CHIANTI emissivity package. Finally, we discuss the estimated behavior of the "Sun as a star" as seen through *ROSAT*.

2. COMPARING THE *ROSAT*-PSPC AND *SNOE*-SXP DATA SETS

2.1. *ROSAT-PSPC*

The *ROSAT*-PSPC instrument and its in-orbit performance are described by Briel & Pfeffermann (1995). The following summarizes details relevant to our study. A cosmic X-ray photon, captured by the main grazing incidence telescope, enters the detector through a thin plastic window; the photon is then photoelectrically absorbed by a counter gas, producing a photoelectron with kinetic energy roughly proportional to the energy of the incoming photon. Thermalization of the photoelectron by collisions with other counter gas atoms yields a secondary electron/ion cloud whose number of electrons is proportional to the initial photon energy. The secondary electrons are attracted to a high-voltage anode where they excite a tertiary ionization avalanche cloud whose charge induces signals at other anodes and cathodes in the detector, ultimately recorded as a digital pulse. The detector's quantum efficiency is mostly determined by the transmission of the window foil and the support grid. The presence of carbon in the window produces a large dip at the carbon edge near 44 Å (0.28 keV; see Fig. 1). The detected pulses are sorted into bins according to their strengths ("pulse-height channels"), which allows a crude estimate of the energy spectrum to be recovered. If we denote one such channel with label i, the count rate in this channel is

$$C_i = \int R_{i\epsilon} a_\epsilon f_\epsilon \, d\epsilon \, , \tag{1}$$

where ϵ is the energy at which the incident spectrum f_ϵ is specified (in units of photons cm^{-2} s^{-1} erg^{-1}), a_ϵ is the effective area (in units of cm^2), and $R_{i\epsilon}$ is a redistribution function. The latter describes the redistribution of the input photon spectrum into the *ROSAT*-PSPC pulse-height channels and is given as a matrix by the *ROSAT* project. It satisfies, for all ϵ,

$$\sum_i R_{i\epsilon} = 1 \, . \tag{2}$$

This function (when discretized in ϵ to form a matrix) has a broad diagonal structure, indicating that photons incident at a certain energy are most likely to be registered at a range of pulse-height channels centered at that energy, but with a significant spread $\Delta\epsilon$ such that $\epsilon/\Delta\epsilon \sim 1$. Not all elements of the matrix are precisely known, limiting the accuracy with which spectral information can be extracted from the measurements. The best-known parts of the matrix lie in subsets of the 256 output channels. Following convention, we define count rates for the passbands called R, S, and H as

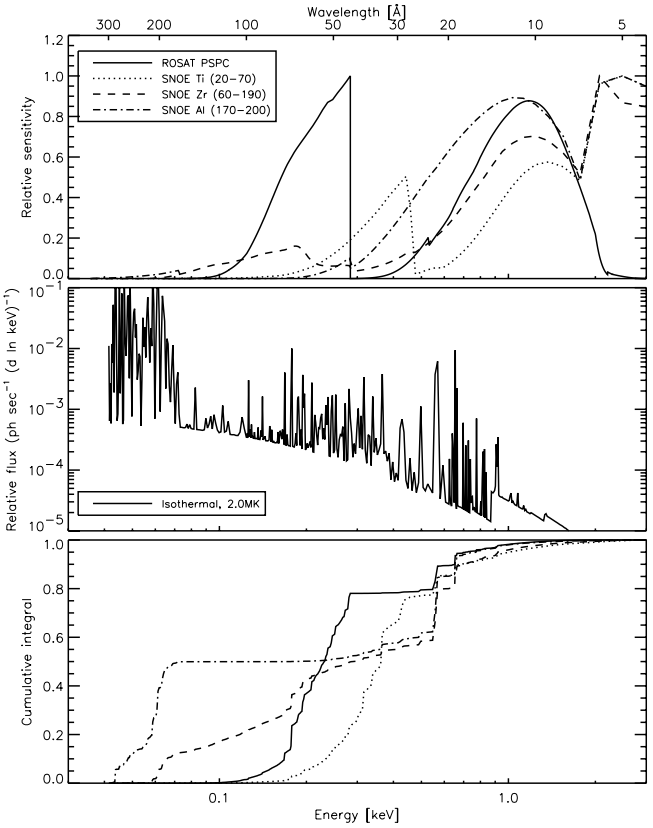

FIG. 1.—Relative effective areas a_ϵ of the *ROSAT*-PSPC and *SNOE*-SXP channels (*top*), an isothermal spectrum f_ϵ computed using version 3.03 of the CHIANTI package (*middle*), and cumulative integrals $I(E) = \int_0^E a_\epsilon f_\epsilon \, d\epsilon / \int_0^\infty a_\epsilon f_\epsilon \, d\epsilon$ (*bottom*). While there is some overlap between *ROSAT*-PSPC and the *SNOE*-SXP channels, they are qualitatively different.

$$R = \sum_{i=10}^{240} C_i = \sum_{i=10}^{240} \int R_{i\epsilon} a_\epsilon f_\epsilon \, d\epsilon \, , \tag{3}$$

$$S = \sum_{i=11}^{41} \int R_{i\epsilon} a_\epsilon f_\epsilon \, d\epsilon \, , \tag{4}$$

$$H = \sum_{i=52}^{201} \int R_{i\epsilon} a_\epsilon f_\epsilon \, d\epsilon \, , \tag{5}$$

where R is proportional to the flux of soft X-rays between energies of 0.1 and 2.4 keV (5–124 Å), and H and S define previously adopted hard and soft channels, respectively (Schmitt, Fleming, & Giampapa 1995). The latter have been used to define a "hardness ratio" as

$$\mathrm{HR} = \frac{H - S}{H + S} \, . \tag{6}$$

The sum in equation (3) for channel R corresponds to that used in the *ROSAT* All-Sky Survey (RASS); in particular, it

applies to the count rates used by Hünsch et al. (1998, 1999), adopted by us below. J. H. M. M. Schmitt (2002, private communication) estimates an uncertainty of ±10% for the *ROSAT*-PSPC effective areas.

2.2. *SNOE-SXP*

The *SNOE*-SXP instrument and its performance are described by Bailey et al. (2000). In brief, the instrument consists of three silicon diodes sensitive in the soft X-ray to extreme-ultraviolet wavelength range (XUV), with different filter materials deposited directly on the diode surfaces. A photon of energy $3.65n$ eV (i.e., at wavelength $3400/n$ Å) that passes through each filter onto a diode surface yields, if absorbed, n electrons in the diode's conduction band. Each photometer's bandpass is determined by its thin film coating, which has been especially designed to reject the intense solar light longward of 300 Å. Thus, for a given voltage applied to the diode, the current is proportional to the solar energy flux per unit time, integrated over the appropriate waveband and the area of the diode.

The first diode has a Ti coating that, when folded with typical solar spectra, transmits photons of energies mostly between 0.18 and 0.62 keV (i.e., 20–70 Å) (Bailey et al. 2000, their Fig. 4; see also our Fig. 1). The second has a Zr/Ti/C coating with an effective passband mostly between 0.07 and 0.21 keV (60–190 Å), and the third has an Al/C coating with a passband between 0.062 and 0.073 keV (170–200 Å). All the diodes have sensitivities to photons at higher energies, as can be seen in the *SNOE*-SXP response curves shown in Figure 1. Coupled with the shape of the solar spectrum outside of flares, this means that the diodes' responses all lie mostly in the energy ranges listed above.

The photodiode coatings have small imperfections, rendering the currents sensitive to the (much larger) flux of solar UV photons through these defects. These contributions to the currents must be measured and subtracted from the data. This is done by periodically placing a fused silica window in front of the diodes to absorb the XUV light, leaving only the softer, UV component (see Bailey et al. 2000, their Fig. 2). During the first 2 years of the mission (when the data used in this paper were taken), the *SNOE*-SXP made an X-ray measurement on every fourth orbit, or approximately 4 times per day. On the other orbits, approximately 12 per day, a measurement with the fused silica window was performed to obtain the UV/visible background. These measurements showed that the window transmission and UV/visible light leaks were very stable. Later in the mission, the fused silica window measurement frequency was reduced to 1 orbit per day. The *SNOE*-SXP diodes have thus been carefully calibrated, yielding rms uncertainties of ±23% for the Ti-coated diode and ±15% for the Zr/Ti/C and Al/C diodes, within the nominal bandpasses noted above.

Let f_ϵ be the flux density of soft X-ray photons incident on the *SNOE*-SXP diodes. The electrical current J_i measured in diode i is

$$J_i = \int_{\epsilon_1^i}^{\epsilon_2^i} a_\epsilon^i f_\epsilon \, d\epsilon \ , \tag{7}$$

where a_ϵ^i is the sensitivity function, whose shapes are shown in Figure 1. Equation (7) serves to define an effective area a_ϵ^i for each diode in terms of the current per unit incident flux density, instead of the more familiar count rate per unit flux density given by equations (3)–(5).

2.3. *Tying the ROSAT-PSPC and SNOE-SXP Data Sets Together*

Equation (7) for the current measured by *SNOE*-SXP is of essentially the same form as equations (3)–(5) for the count rates measured by the *ROSAT*-PSPC instrument, except for the redistribution function $R_{i\epsilon}$ in equations (3)–(5). The formalisms are identical when the sum over pulse-height channels extends over the entire *ROSAT*-PSPC range, because of equation (2). Summing over the narrower ranges in the *ROSAT*-PSPC pulse-height channels given by equations (3)–(5) leads to a well-defined set of count rates for a given input spectrum and has the benefit that these subsets are more accurately calibrated (i.e., $R_{i\epsilon}$ is better known) than for the channels outside of these ranges.

Figure 1 shows curves proportional to the effective areas of the *ROSAT*-PSPC and *SNOE*-SXP instruments, a theoretical spectrum f_ϵ computed using the latest version (3.03) of the CHIANTI package (see below), and the cumulative contributions to the total count rates (*ROSAT*-PSPC) and currents (*SNOE*-SXP). The *ROSAT*-PSPC and *SNOE*-SXP instruments obviously measure different properties of the solar and stellar spectra f_ϵ, but the bottom panel of Figure 1 shows that the *SNOE*-SXP channels span the sensitivity range of *ROSAT*-PSPC to the energy of this particular input spectrum. Note that f_ϵ—or at least some spectrally integrated property of f_ϵ—is *the* information about the Sun and stars that we would like to compare directly. To compare data sets from such different instruments requires additional information on f_ϵ. Such information is added using synthetic spectra.

First, we normalize each flux density f_ϵ to that projected down onto the stellar surface F_ϵ using

$$F_\epsilon = \frac{d^2}{R_*^2} f_\epsilon \ , \tag{8}$$

where R_* is the stellar radius and d is the distance to the star. Next, we define average flux densities that can be derived directly from the count rates and currents measured by the two instruments. For the ith diode of *SNOE*-SXP, a suitable average can be defined as

$$\langle F^i \rangle = \frac{\int_{\epsilon_1^i}^{\epsilon_2^i} a_\epsilon^i F_\epsilon \, d\epsilon}{\int_{\epsilon_1^i}^{\epsilon_2^i} a_\epsilon^i \, d\epsilon} \text{ photons cm}^{-2} \text{ s}^{-1} \text{ erg}^{-1} \ . \tag{9}$$

With

$$A^i = \int_{\epsilon_1^i}^{\epsilon_2^i} a_\epsilon^i \, d\epsilon \text{ cm}^2 \text{ ergs} \ , \tag{10}$$

a quantity that is determined only by instrumental properties, equations (7) and (8)–(10) give

$$\langle F^i \rangle = \frac{d^2}{R_*^2} \frac{1}{A^i} J_i \text{ photons cm}^{-2} \text{ s}^{-1} \text{ erg}^{-1} \ . \tag{11}$$

By analogy, for the *ROSAT*-PSPC instrument, we can write from equations (3)–(5), for the ith passband,

$$\langle F^i \rangle = \frac{1}{A^i} \sum_{j=\min}^{\max} \int R_{j\epsilon} a_\epsilon F_\epsilon \, d\epsilon, \tag{12}$$

where

$$A^i = \sum_{j=\min}^{\max} \int R_{j\epsilon} a_\epsilon \, d\epsilon \tag{13}$$

and where "min" and "max" specify the lower and upper limits of the summed *ROSAT*-PSPC pulse-height channels for the *i*th passband, whence

$$\langle F^i \rangle = \frac{d^2}{R_*^2} \frac{1}{A^i} C_i \text{ photons cm}^{-2} \text{ s}^{-1} \text{ erg}^{-1} . \tag{14}$$

Equations (11) and (14) are both of the form

$$\langle F^i \rangle = \frac{d^2}{R_*^2} \frac{1}{A^i} M_i \text{ photons cm}^{-2} \text{ s}^{-1} \text{ erg}^{-1} , \tag{15}$$

where the measured quantities M_i are C_i for *ROSAT*-PSPC and J_i for *SNOE*-SXP. By definition, $\langle F^i \rangle$ measures a weighted average of the surface flux density, where the weighting function is the effective area of the *SNOE*-SXP diode or the effective area and redistribution function for the particular *ROSAT*-PSPC passband. Given A^i and measurements of M_i, equation (15) contains everything needed to determine $\langle F^i \rangle$ for channel i of either instrument. It is important to note that, for a given instrument, *this equation can be used to determine* $\langle F^i \rangle$ *from the measurements* M_i *independently of any assumptions concerning the shape of the spectrum.*

Our next step—the central aspect of this work—is *to derive theoretical relationships between the mean flux densities* $\langle F^i \rangle$ *for the commonly used passbands for ROSAT and the three channels of SNOE.* We do this using sets of synthetic spectra ($F_\epsilon = S_\epsilon$) to compute $\langle F^i \rangle$ in equations (9) and (12). The synthetic spectra S_ϵ were computed using version 3.03 of the CHIANTI package (Dere et al. 2001).

Coronal X-ray emission is dominated by optically thin Bremsstrahlung and emission lines (with smaller contributions from photoionization continua), all of which arise from collisions involving thermal electrons. Thus, we compute mean flux densities from series of spectra computed under isothermal conditions. While both S_ϵ and $\langle F^i \rangle$ depend also on electron pressure P_e, the shape of the spectrum depends far more strongly on electron temperature T_e, particularly when integrated over channels covering many spectral lines, as are considered here. When the X-ray spectrum from an entire corona is mostly optically thin, it can simply be computed as a sum of spectra of isothermal plasmas with an appropriate weighting. Our approach is therefore as follows:

1. Compute $S_\epsilon(T_e)$ from isothermal plasmas as a function of T_e between 5×10^5 and 2×10^7 K.

2. Determine mean flux densities $\langle F^i \rangle$ in *ROSAT* and *SNOE* passbands from the computed $S_\epsilon(T_e)$, as a function of T_e, using equations (9) and (14).

3. Find linear combinations of the *SNOE* mean flux densities that approximate the *ROSAT* mean flux densities:

$$\langle F^i \rangle_{ROSAT}(T_e) \approx \sum_{j=1}^{3} c_{ij} \langle F^j \rangle_{SNOE}(T_e) ,$$
$$10^6 \text{ K} < T_e < 2 \times 10^7 \text{ K} . \tag{16}$$

4. Convert the *SNOE*-SXP measured currents to $\langle F^i \rangle_{SNOE}$ from equation (11), and use equation (16) to estimate $\langle F^i \rangle_{ROSAT}$, which can be compared with stellar measurements through equation (14). Conversion to energy flux densities and luminosities requires further use of the synthetic data and is discussed in § 2.4.

5. Evaluate the influence of pressure and elemental abundance variations within the coronal plasma on the results (coronal abundance variations are reviewed, for example, by Feldman 1998).

To determine the coefficients c_{ij} we minimized the residual

$$R^i = \frac{1}{n} \sum_{k=1}^{n} \left| \langle F^i \rangle_{ROSAT}(T_k) - \sum_{j=1}^{3} c_{ij} \langle F^j \rangle_{SNOE}(T_k) \right|^2 \tag{17}$$

for each *ROSAT*-PSPC passband i. The optimization was done numerically using an IDL version of the genetic algorithm (GA) PIKAIA (Charbonneau & Knapp 1995) kindly provided by S. McIntosh (2002, private communication).[2] The sum over temperatures from T_1 to T_n included a grid of temperatures linear in $\log T_e$, from 10^6 to 2×10^7 K. This temperature range was chosen to encompass contributions from solar-like quiet and active regions (e.g., Vaiana & Rosner 1978; Haisch & Schmitt 1996).

In the Appendix, we discuss sources of error in this approach, which hinge on three issues: the accuracy of the model spectra, uncertainties introduced via abundance variations, and the quality of the fit given by equation (16). While there remain unquantifiable, but potentially important, sources of error arising from the first two considerations, those arising from the quality of the fit are shown there to be ±15% or less. Figure 2 shows two typical calculations of $\langle F \rangle(T_e)$ for the RASS passband (0.1–2.4 keV). In these calculations two sets of abundances were adopted, from Allen (1973) and from Feldman et al. (1992b), and a constant electron pressure of 10^{15} cm^{-3} K was assumed. In these cases, between 10^6 and 10^7 K, the linear combination of *SNOE*-SXP channels can reproduce the *ROSAT*-PSPC soft channel's behavior with an rms variation ($\sqrt{R^i}$ in eq. [17]) of ≈14% of $\langle F^i \rangle$. This relatively small variation shows that, provided the synthetic data are qualitatively reasonable, the *SNOE* measurements can be translated into equivalent *ROSAT*-PSPC RASS count rates with this level of accuracy. These rms variations should be considered as upper limits because they relate to isothermal calculations. Stellar spectra are better characterized by a distribution of material at different temperatures, which serves to average out these variations.

Fits, not shown here, for electron pressures factors of 10 smaller and larger have very similar coefficients. The fits for the other passbands differ not only in the coefficients but also in the quality of fit, as measured by the rms fluctuations. The *S* passband (0.1–0.4 keV) fits show rms fluctuation variations of 12%–32% about calculated values, the worse fits corresponding to calculations using coronal abundances. For the *H* passband (0.5–2 keV), the rms variations are between 20% and 29%, and examples are shown in Figure 12 in the Appendix. However, for the *H* passband, an additional source of error arising from uncertainties in the

[2] Simple linear projection using Gram-Schmidt orthogonalization yielded very similar results. The GA yields slightly smaller residuals.

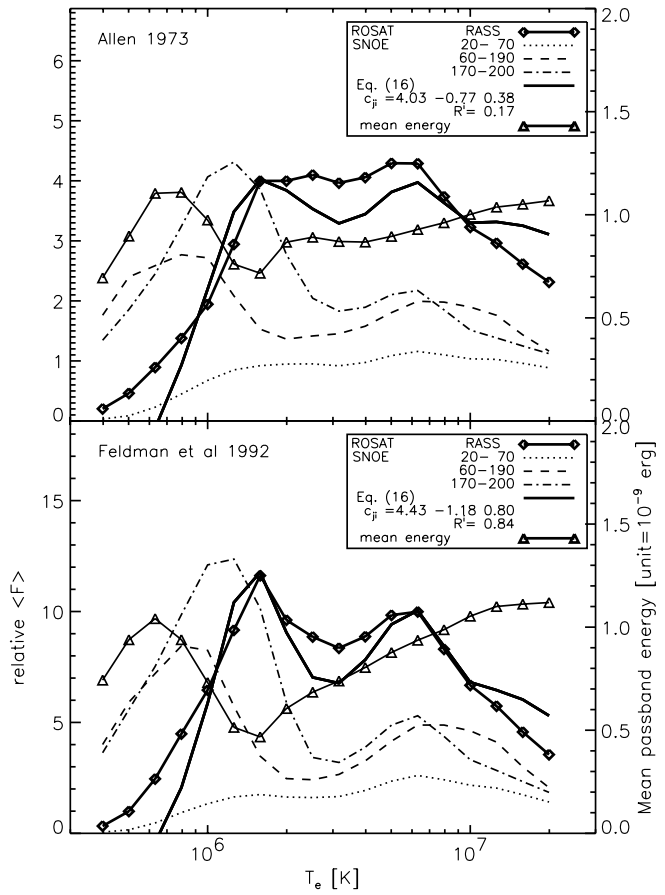

FIG. 2.—Mean flux densities in arbitrary units (given by eqs. [9] and [12]) computed as a function of electron temperature T_e for the RASS (0.1–2.4 keV) *ROSAT*-PSPC passband and the three *SNOE*-SXP channels. Abundances were taken from Allen (1973) (*top*), and from Feldman et al. (1992a) (*bottom*). The electron pressure was $p_e T_e = 10^{15}$ cm^{-3} K in both cases. The thick solid line shows the linear combination of *SNOE*-SXP channels that most closely mimics the *ROSAT*-PSPC temperature dependence, as given by eq. (16). The legend lists the fit parameters and residual in eq. (17). Also shown (and measured on the right axis) is the mean passband energy $\langle \epsilon^i \rangle$ (defined through eq. [21]).

poorly known *SNOE*-SXP effective areas at energies higher than the nominal passbands limits the usefulness of equation (16). Such fits are very sensitive to these high-energy values. For this reason we cannot trust conversions from *SNOE*-SXP to *ROSAT*-PSPC for the *H* passband.

2.4. *Energy Flux Densities and X-Ray Luminosities*

Our use of photon flux densities enables us to use equations such as equations (11) and (14) to link the *ROSAT*-PSPC and *SNOE*-SXP data sets via equation (16). However, essentially all of the literature deals with energy flux densities and luminosities. Therefore, some estimate of the energy flux densities is required. Starting with the measured *SNOE*-SXP currents, two approaches are possible. First, we note that equations (9) and (16) yield

$$C_i \approx \frac{d_\odot^2}{d^2} A^i_{ROSAT} \sum_{j=1}^{3} c_{ij} \frac{J_j}{A^j_{SNOE}} \ , \qquad (18)$$

where $d_\odot$ is the Sun-Earth distance, allowing us to convert the *SNOE*-SXP net current densities J_j approximately into count rates in *ROSAT*-PSPC's passband i, if the Sun were placed at a distance d from the Earth. This approach could be used directly to simulate the count rates and hardness ratios employed in earlier work in which luminosities were computed directly from these quantities. As an example, the data sets compiled by Hünsch et al. (1998, 1999) used results from spectral calculations of Fleming et al. (1995) to estimate stellar energy flux densities as functions of count rates and hardness ratios, based on calculations using the emissivities of Raymond & Smith (1977). These calculations yielded

$$f_{\rm RASS} = [5.30({\rm HR}) + 8.31] \times 10^{-12} C_{\rm RASS} \text{ ergs cm}^{-2} \text{ s}^{-1} \quad \text{(Raymond-Smith)} \ , \qquad (19)$$

where HR is defined in equation (6), $C_{\rm RASS}$ is the count rate determined in the RASS (0.1–2.4 keV) passband, and the energy flux density $f_{\rm RASS}$ (ergs cm^{-2} s^{-1}) is the estimated energy flux in the same passband. The stellar luminosity in this passband is simply

$$L_{\rm RASS} = 4\pi d^2 f_{\rm RASS} \ . \qquad (20)$$

Instead of applying equations (18)–(20) directly, a second approach is more desirable for estimating the solar luminosity in a given passband from *SNOE*-SXP data, from two points of view. First, as noted above, counts in the *H* bandpass, and hence the hardness ratios, are not accurately determined from *SNOE*-SXP. Second, the approach outlined above combines calculations from two theoretical models, so it lacks internal consistency. Instead, we use the CHIANTI calculations to get directly the energy conversion factors through the relation

$$E^i = \int_{\epsilon_1^i}^{\epsilon_2^i} F_\epsilon \epsilon \, d\epsilon = \langle F^i \rangle (\epsilon_2^i - \epsilon_1^i) \langle \epsilon^i \rangle \text{ ergs cm}^{-2} \text{ s}^{-1} \ , \qquad (21)$$

which simply defines the mean energy in channel i, $\langle \epsilon^i \rangle$, in terms of the total energy flux density in the channel, E^i, and other quantities introduced earlier. Given E^i, X-ray luminosities $L^i_{\rm X}$ are simply

$$L^i_{\rm X} = 4\pi R_*^2 E^i \text{ ergs s}^{-1} \ . \qquad (22)$$

Our preferred approach is thus to evaluate $\langle \epsilon^i \rangle$ using the theoretical calculations in equation (21). Measured currents and count rates are converted to $\langle F^i \rangle$ using equations (18) and (14). Equations (21) and (22) then yield solar and stellar X-ray flux densities and luminosities.

The accuracy of this approach, in common with all earlier stellar X-ray work, hinges on the accuracy of the theoretical spectra and the relative constancy of $\langle \epsilon^i \rangle$ with T_e, which is also shown in Figure 2. The top panel shows results for the RASS bandpass computed using the photospheric abundances of Allen (1973). The function $\langle \epsilon^i \rangle$ varies remarkably little with T_e, showing a weak, almost monotonic increase with T_e above 10^6 K. A linear fit of the computed values of HR and $\langle \epsilon^i \rangle$ yields, for calculations done with $T_e \geq 10^6$ K, in analogy to equation (19),

$$f^*_{\rm RASS} = [1.40({\rm HR}) + 8.32] \times 10^{-12} C_{\rm RASS} \text{ ergs cm}^{-2} \text{ s}^{-1} \quad \text{(Allen abundances)} \ . \qquad (23)$$

Similarly, for the bottom panel of Figure 2, which is based

on abundances of Feldman et al. (1992b), we find

$$f^{*}_{\rm RASS} = [2.95({\rm HR}) + 7.61] \times 10^{-12} C_{\rm RASS} \ {\rm ergs\ cm^{-2}\ s^{-1}} \quad ({\rm Feldman\ abundances})\ . \quad (24)$$

The CHIANTI results yield a less steep dependence of the energy flux densities on the hardness ratio than those computed using the earlier Raymond-Smith model. Figure 3 compares X-ray luminosities in the RASS bandpass computed using equations (19) and (23), from count rates and hardness ratios tabulated by Hünsch et al. (1998). The systematic offset between these two calculations simply reflects the differences between equations (19) and (23). This highlights the need for internal consistency and emphasizes that energy flux budgets are more difficult to evaluate than photon flux budgets. Finally, we note that equations (19), (23), and (24) can be applied to the measured *ROSAT*-PSPC data but not to the *ROSAT*-PSPC data that have been derived via equation (18), simply because the *SNOE*-SXP data cannot yield reliable values of HR. Hence the use of the asterisk superscript in equations (23) and (24). Therefore, for the solar data, we use

$$f^{\odot}_{\rm RASS} = (8.1 \pm 0.9) \times 10^{-12} C_{\rm RASS} \ {\rm ergs\ cm^{-2}\ s^{-1}} \quad ({\rm Allen\ abundances})\ , \quad (25)$$

with $L^{\odot}_{\rm RASS} = 4\pi d^{2}_{\odot} f^{\odot}_{\rm RASS}$. The constants in equation (25) come from the mean value and rms variation of $\langle \epsilon^{i} \rangle$ above 10^{6} K, as shown in the top panel of Figure 2. For comparison, the numerical constant[3] derived using the abundances of Feldman et al. (1992b) is $(7.4 \pm 2.0) \times 10^{-12}$ ergs cm^{-2} count^{-1}.

[3] All these calculations are similar to those used by earlier workers. For example, it is reassuring that our CHIANTI calculations applied to the *Einstein* IPC instrument yield a numerical conversion factor of 1.7×10^{-11} ergs cm^{-2} count^{-1}, identical to that used by Schrijver (1983).

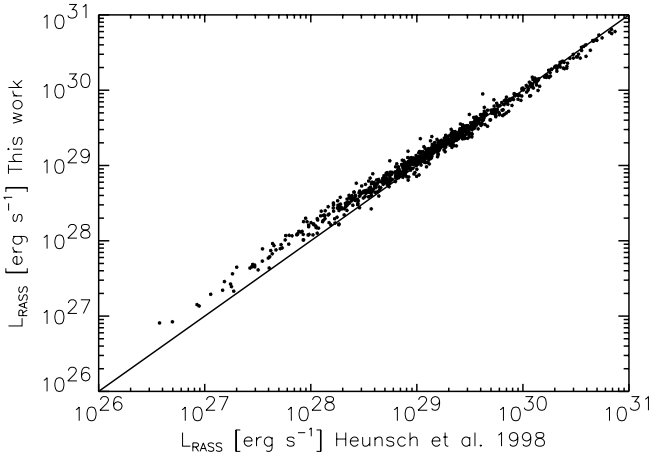

FIG. 3.—X-ray luminosities in the RASS passband computed using the earlier energy budget calculations based on the Raymond-Smith code (*abscissa*) and on the CHIANTI calculations in this paper (*ordinate*). *ROSAT*-PSPC count rates and hardness ratios were taken from Hünsch et al. (1998). The solid line represents equality. The different slopes arise from the different values of the coefficients in eqs. (19) and (23).

3. RESULTS

We examined the *SNOE*-SXP net currents in the three channels that were obtained for the first 545 days following the launch of the *SNOE* satellite on 1998 March 11. The minimum of the solar magnetic activity cycle occurred in 1997 January or so. Thus, the *SNOE*-SXP data set does not sample a representative minimum in solar magnetic activity, and so below we include some extrapolations of the *SNOE*-SXP measurements. Fortunately, the data were acquired during the steepest part of the cycle. The Ottawa radio emission at 10.7 cm ("F10.7," measured in the usual "solar flux units" of 10^{-19} ergs s^{-1} cm^{-2} Hz^{-1}) varied from 80 to 270 during this period, with 96% of the F10.7 values containing between 95 and 210. Only rarely does F10.7 exceed 300; at solar minimum it is $\approx$65. Thus, the *SNOE*-SXP data set did sample a significant fraction of the solar cycle.

The measured currents are shown in Figure 4, together with X-ray luminosities predicted for the RASS bandpass, for two sets of abundances. These were evaluated using equation (18) to get the equivalent count rates only for the RASS bandpass, and then equation (25) (and its equivalent for the other abundance data set). The uncertainties plotted include those in the *SNOE*-SXP effective areas and the rms variation of the mean energy $\langle \epsilon^{i} \rangle$ with T_e. Several features in the figure are of interest. First, the conversion preserves the overall form of the *SNOE*-SXP current variations. This is because of the linear relationship between these quantities built into equation (18). Second, the summation does not suffer unduly from cancellation, so that propagated

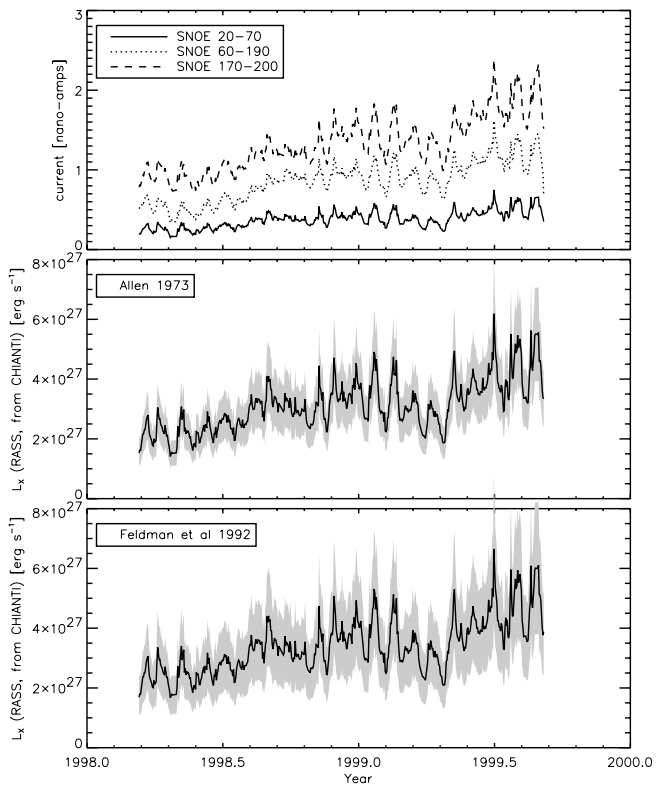

FIG. 4.—*Top*: Net currents measured in the three *SNOE*-SXP diodes plotted as a function of time. *Middle and bottom*: Equivalent X-ray luminosities as would have been measured by *ROSAT*-PSPC in the RASS bandpass, for two cases of the assumed abundances. The shaded areas mark the estimated uncertainties.

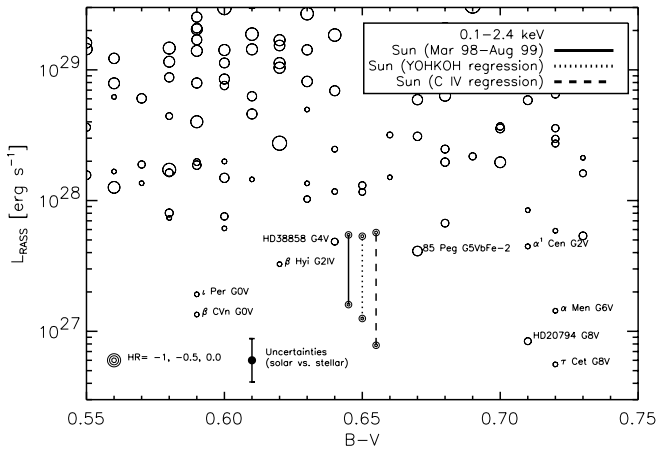

FIG. 5.—Estimated ranges of X-ray luminosities in the RASS passband for the Sun compared with stellar values from the *ROSAT*-PSPC database compiled by Hünsch et al. (1998), plotted against the Johnson $B-V$ color index taken from the same database. The circle sizes are proportional to the measured hardness ratios, and the three lines delimit the central 96% of the predicted solar luminosity distribution functions, to remove outlying points. Note that the Sun lies at the lowest activity levels among this sample because the sample is drawn from a brightness-limited, not volume-limited, data set.

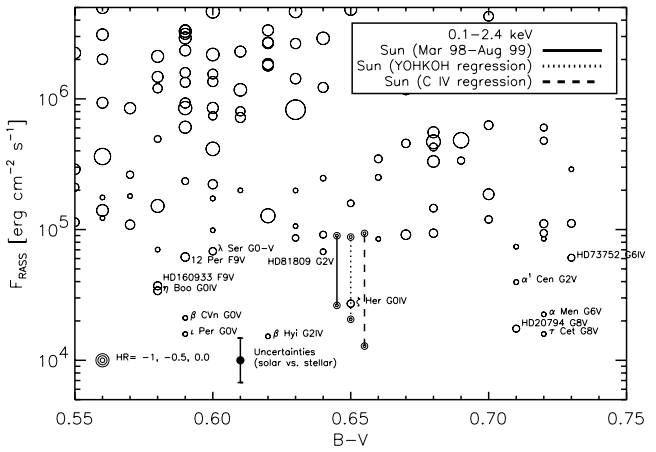

FIG. 6.—Similar to Fig. 5, except that X-ray surface flux densities are plotted on the ordinate. The stellar sample is drawn from a brightness-limited data set.

uncertainties are not overwhelming and are 27% and 35% for the two abundance sets, respectively. Third, the conversion predicts significant rotational and solar cyclic modulation of the Sun as seen through the RASS passband of *ROSAT*-PSPC (this is quantified below). Finally, we see that within the estimated uncertainties the results are essentially identical for the two quite different sets of abundances.

A comparison between *ROSAT*-PSPC stellar luminosities and the solar behavior predicted for the RASS passband is shown in Figure 5, where the abundances of Allen (1973) are used. The figure includes those stars with $B-V$ colors between 0.55 and 0.75 in the data set of nearby dwarf and subgiant stars from Hünsch et al. (1998). *ROSAT*-PSPC count rates and *Hipparcos* distances were taken directly from Table 2 of Hünsch et al. (1999), and equation (23) was used to evaluate luminosities. The error bars include the uncertainties in the *ROSAT*-PSPC and *SNOE*-SXP effective areas and the uncertainty given in equation (25). Uncertainties in distances are in general small for this population of stars, of which 90% of this subset are closer than 50 pc, and 65% are closer than 25 pc. They are negligible compared with the propagated uncertainties from the other sources. For example, a typical *Hipparcos* uncertainty is less than $[d\,(\mathrm{pc})/5]\%$ (Arenou et al. 1995), translating to an additional uncertainty in L_X of less than 20% for 90% of the stars in this sample. Figure 6 compares the surface flux densities, where values of d/R_* were derived from the surface brightness versus $B-V$ relationship of Barnes, Evans, & Moffett (1978). The error bars are larger for this plot because this relationship has an intrinsic uncertainty of $\pm 22\%$ in the ratio of d^2/R_*^2 for stars of this color range. Figures 7 and 8 compare histograms of the luminosities and flux densities plotted for the variation over that part of the solar cycle observed by *SNOE*-SXP and for the same sample of stars. Very similar results are found for the sample of stars selected by Hünsch et al. (1999), which consists of a nearly complete sample of all stars within 25 pc of the Sun. It is unfortunate that the predicted Sun's luminosity in the RASS band is as low as 10^{27} ergs s^{-1}, because the detection limit of the RASS observations is typically just $10^{27.9}[d/(25\ \mathrm{pc})]^2$ ergs s^{-1}. Thus, at the level of sensitivity needed to detect solar X-ray emission throughout most of the solar activity cycle, the sample is complete only within $d = 9$ pc, where there are just three stars with $0.55 < B-V < 0.75$ (HD 10700 = τ Cet, HD 20794, and HD 128620 = α Cen A). RASS was simply not sensitive enough to make quantitative comparisons of the solar and stellar distributions shown in Figures 7 and 8: a survey twice as sensitive would have captured 16 stars in this color range. In § 4.2 we compare the solar luminosity distribution function with one determined from a volume-limited sample of nearby G stars by Schmitt (1997). Schmitt's fit to this

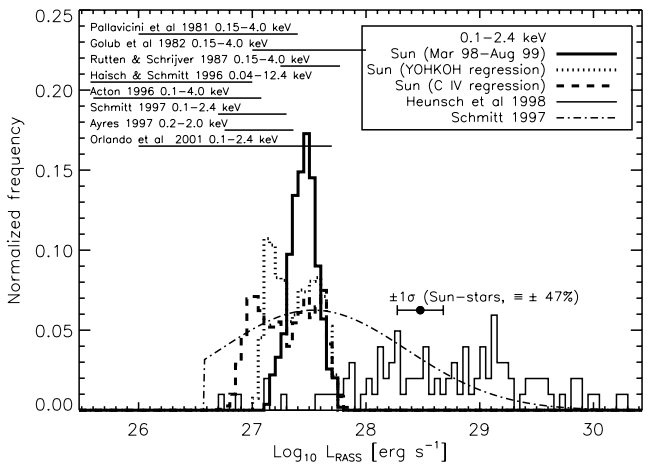

FIG. 7.—Histograms showing the predicted X-ray luminosity of the Sun as seen in the RASS bandpass of the *ROSAT*-PSPC instrument, among the distribution of nearby stars with $B-V$ colors between 0.55 and 0.65 in the data set of Hünsch et al. (1998). Only main-sequence stars and subgiants are included, amounting to just 120 stars, in this color range. The ranges of X-ray luminosities derived in earlier work are shown as horizontal lines, annotated with references and the relevant bandpasses. The smooth dot-dashed curve shows Schmitt's (1997) fit to his volume-limited sample of nearby G stars, truncated at the lowest luminosities (no stars were found for such low values). The difference between Schmitt's curve and the histogram of Hünsch et al. (1998) arises from the fact that the latter is a brightness-limited sample.

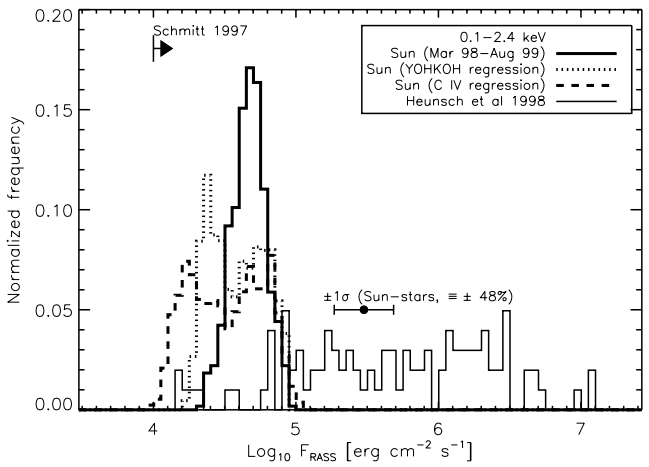

FIG. 8.—Similar to Fig. 7, except that histograms of the X-ray surface flux densities are plotted on the ordinate. The same subset of stars is extracted from the sample of Hünsch et al. (1998) as in Fig. 7. The arrow marked "Schmitt 1997" shows the lower limit of X-ray surface flux densities found for stars, identical to that found by Schmitt (1997) for the Sun covered with coronal hole plasma.

distribution function is shown as the dot-dashed curve in Figure 7. The figure shows that the Sun's behavior derived from the *SNOE*-SXP measurements is typical of nearby G stars, but if the extrapolated data are to be believed, the Sun's average X-ray luminosity may be a factor of $\approx$2 smaller than the broad peak of Schmitt's (1997) distribution.

3.1. *Extrapolations*

To estimate further the solar cyclic variations, we must look to additional data. A minimum value of the luminosity in the RASS bandpass can be estimated from earlier data sets. In data collected by Manson (1977), the solar luminosity in the RASS bandpass does not drop below $10^{26.8\pm0.3}$ ergs s^{-1} for F10.7 values even as low as 81 (see § 4.1). This is substantially higher than the estimates of $10^{25.5}$ to 10^{26} based on *Yohkoh*-SXT data and models mentioned in § 1.

A second way to estimate the cyclic variation is extrapolation using regressional analysis with other data sets. Estimates were therefore made through linear regression fits of the *SNOE*-SXP data and two sets of data for which complete and accurately calibrated solar cyclic behavior are available. The first (not shown in the figures here) is the 10.7 cm radio flux that has been measured at least once daily since 1947. Outside of flares, the radio measurements arise from free-free emission in the corona. F10.7, when filtered to remove occasional radio "flares," is strongly correlated with EUV irradiance measurements (Manson 1977; Walker 1977). The *SNOE*-SXP irradiance data are no exception (see Fig. 7 of Bailey et al. 2000), showing correlation coefficients of $\approx$0.9 (see Table 1). The second data set is the irradiance of the C IV $\lambda\lambda$1548, 1550 doublet observed with the SOLSTICE instrument on the *Upper Atmosphere Research Satellite* since 1991, for which accurate daily values are available (T. Woods 2002, private communication). The C IV feature arises in the subcoronal "transition region" at a temperature of $\sim10^5$ K. Stellar data have revealed statistical correlations between X-ray and C IV emission (e.g., Ayres, Marstad, & Linsky 1981; Schrijver 1987; Rutten et al. 1991). Both the F10.7 and C IV data sets were filtered using a running median to remove outliers before making the linear regression. Figure 9 shows the linear regression between the *SNOE*-SXP Ti (20–70 Å) diode's current and the C IV irradiances.

TABLE 1

CORRELATION COEFFICIENTS BETWEEN THE *SNOE*-SXP 20–70 Å CHANNEL AND THE OTHER DATA SETS

Data Set	Pearson	Spearman
F10.7	0.895	0.899
SOLSTICE C IV	0.913	0.919
Yohkoh-SXT 80–20 Å	0.867	0.870

Both of the above data sets have more accurate calibrations than the *SNOE*-SXP data themselves. They suffer, however, from being only indirectly related to X-ray emission. Therefore a third data set, with substantially higher calibration uncertainties, was regressed against the *SNOE*-SXP data set. *Yohkoh*-SXT obtained imaging data from 1991 October to 2001 April. L. W. Acton (2003, private communication) kindly provided daily averaged estimates of X-ray luminosities in three bins, between 1 and 8 Å, 8 and 20 Å, and 20 and 40 Å, extracted from the raw *Yohkoh*-SXT data, from accompanying models. The highest correlations with the *SNOE*-SXP 20–70 Å diode's current were actually found for the *Yohkoh*-SXT 8–20 Å channel. Correlation coefficients for all three data sets are listed in Table 1. Only linear fits were needed for the F10.7 and SOLSTICE data, but a quadratic fit was required to fit adequately the *Yohkoh*-SXT data, which increase more than linearly with the *SNOE*-SXP currents.

Figures 5–8 include the estimates (*dotted and dashed lines*) using the *Yohkoh*-SXT and SOLSTICE data, extrapolated over at least one complete solar cycle. The results extrapolated from the *Yohkoh*-SXT versus *SNOE*-SXP fit are remarkably similar to those (not shown) from the F10.7 regression. Both the SOLSTICE and *Yohkoh*-SXT extrapolations extend the estimated distribution downward, to 26.8 and 27.0 in the logarithm of $L^{\odot}_{\rm RASS}$, respectively. It is worth noting that $L^{\odot}_{\rm RASS} = 26.8$ ergs s^{-1} corresponds to a surface flux density of 10^4 ergs cm^{-2} s^{-1}, identical to Schmitt's (1997) smallest values found for his volume-limited sample of G stars (see Fig. 8) and to his estimate of the Sun covered with coronal holes based on the analysis of *Yohkoh*-SXT data by Hara et al. (1994).[4] Nevertheless, it is important to stress that all estimates based on extrapolation must be regarded with skepticism.

4. DISCUSSION

4.1. *Comparison with Earlier Estimates of the Solar X-Ray Luminosity*

Figure 7 compares our estimates of solar X-ray luminosities with those from earlier work, spanning cycle minimum

[4] While the minimum value of the X-ray luminosity given by Schmitt (1997) derives from the work of Hara et al. (1994), the origins of the mean and maximum values are unclear. It is interesting that his values, if multiplied by a factor of 4, come into agreement with our new estimates and that a factor of 4 increase is what was found by Solomon, Bailey, & Woods (2001) to convert some standard solar XUV irradiance models to the *SNOE*-SXP measurements.

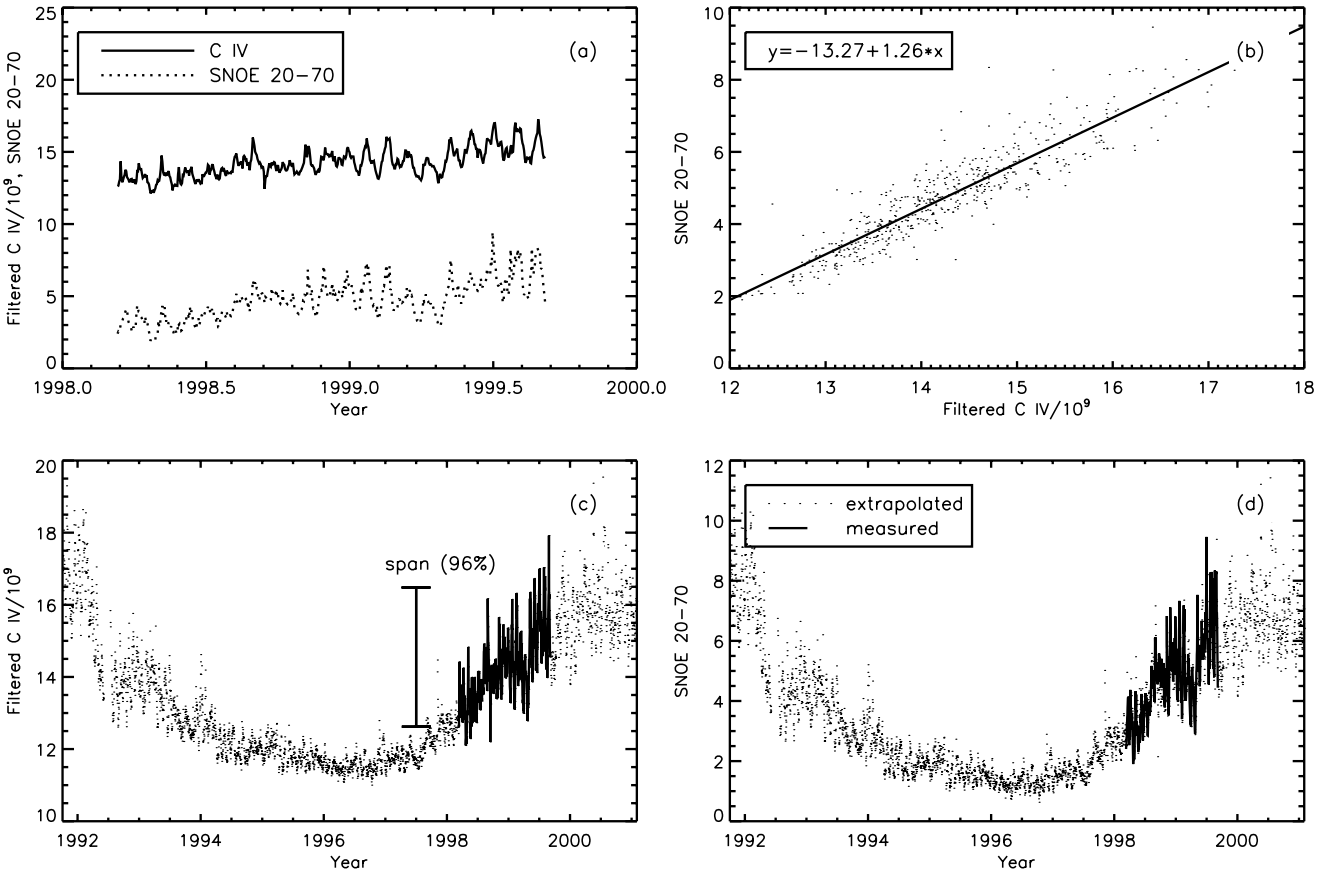

FIG. 9.—Linear regression for the *SNOE*-SXP 20–70 Å diode currents vs. the C IV irradiance (in units of photons cm^{-2} s^{-1}) measured by SOLSTICE. Shown are (*a*) time series, (*b*) the regression, (*c*) filtered C IV time series, and (*d*) the measured (*solid line*) and extrapolated (*points*) *SNOE*-SXP currents for the 20-70 Å channel. In (*c*), the solid line marks the period during which *SNOE* data are available. The barred line marked "span" shows the range of variation seen during this period by the middle 96% of the distribution of measured irradiances.

and maximum, in a variety of passbands. These comparisons also are summarized in Table 2. Note that not all of these earlier results were designed to match the specific *ROSAT*-PSPC response in the manner presented in this paper, so they cannot all be directly, or fairly, compared. Relative to the 0.1–2.4 keV RASS bandpass, our CHIANTI calculations show that the 0.15-4 (*Einstein*) and 0.2-2.0 keV (Ayres's results) bandpass luminosities should be multiplied by factors of roughly 1.1 and 1.6, respectively, and that the 0.04–12.4 keV "bolometric" bandpass of Acton (1996) should be divided by an unknown but substantially larger factor. Applying the known factors, we see that just two of the studies are broadly compatible with our results: that of Ayres (1997) based on suborbital rocket data, and that of

TABLE 2
ESTIMATES OF THE SUN'S X-RAY LUMINOSITY

Passband Name	Passband Energy (keV)	$\log L_{min}$ (ergs s^{-1})	$\log L_{max}$ (ergs s^{-1})	Source	Original Source
Einstein	0.15–4.0	26.0	27.4	1	
Einstein	0.15–4.0	27.0	28.0	2	3
Einstein	0.15–4.0	27.2	27.8	4	5
Bolometric	0.04–12.4	25.5	27.0	6	7
ROSAT	0.1–4.0	25.6	27.1	8	
ROSAT	0.1–2.4	26.7	27.3	9	
ROSAT	0.2–2.0	26.8	27.4	10	
ROSAT	0.1–2.4	26.0	27.7	11	
ROSAT	0.1–2.4	27.1	27.75	12	
ROSAT	0.1–2.4	26.8	27.9	13	

NOTE.—*Einstein* data are for the IPC; *ROSAT* data are for the PSPC.

SOURCES.—(1) Pallavicini et al. 1981; (2) Golub et al. 1982; (3) Vaiana & Rosner 1978; (4) Rutten & Schrijver 1987; (5) Schrijver 1983; (6) Haisch & Schmitt 1996; (7) L. W. Acton 1996, private communication to Haisch & Schmitt; (8) Acton 1996; (9) Schmitt 1997; (10) Ayres 1997; (11) Orlando et al. 2001; (12) this work (1998.2–1999.7); (13) this work (extrapolated over a full solar cycle).

Rutten & Schrijver (1987). The estimates of Golub et al. (1982) can be brought into agreement if divided by ≈2. Schmitt's (1997) work underestimates our luminosities by a factor of 2–3. The remaining studies systematically underestimate our X-ray luminosities during solar minimum and overestimate the solar cyclic variability, and of these only the work of Orlando et al. (2001) matches our estimate under solar maximum conditions.

The origins of the estimates cited in the *Einstein*-IPC studies are all quite vague. While Golub et al. (1982) cite Vaiana & Rosner (1978) as their source, no solar cyclic luminosity estimates can be found in the latter. However, given additional statistical data concerning the coverage of the Sun with coronal holes, quiet features, and active regions, it is possible to construct such estimates from their Table 2, but even so, no specific bandpass is given for these estimates, which hinge on the lowest energy limit of the given bandpass because of the steepness of the spectrum (e.g., see Fig. 1). Interestingly, the somewhat different estimates of Rutten, Schrijver, and colleagues in the table also point to Vaiana & Rosner (1978) as the original source in Table 1A of the paper by Schrijver (1983). The other *Einstein*-related estimate, from Figure 6 of Pallavicini et al. (1981), seems to be based on early irradiance measurements summarized by Kreplin et al. (1977) that focused on the region below 10 Å (i.e., above 1.24 keV) but also discussed data to 20 Å. The bandpass used for this estimate is presumably that of the *Einstein* IPC, 0.15–4 keV, although again this is not clear.

Two of the more recent studies are based on analysis of *Yohkoh*-SXT data, and they disagree significantly with our results. The preliminary estimates of Acton (1996) are all significantly smaller than ours. The luminosity at the maximum of the solar activity cycle given by Orlando et al. (2001) agrees well with our estimate, but their minimum value is significantly smaller. By predicting much smaller luminosities at solar minimum, these authors also predict a factor of 30 variability of the Sun as seen by the *ROSAT*-PSPC 0.1–2.4 keV bandpass, over the solar cycle. These disagreements with our results appear to have a twofold origin.

First, *Yohkoh*-SXT's bandpasses are relatively hard (see Fig. 2 of Stern, Alexander, & Acton 2003), so they miss the soft part of the spectrum below 0.3 keV ($\lambda > 41$ Å), where *ROSAT*-PSPC and *Einstein*-IPC have high sensitivities. Figure 10 shows images of the Sun obtained on 1996 May 13 with instruments on *SOHO* (SUMER, EIT), which imaged the transition region (the λ933 line of S VI, formed near 2×10^5 K) and 10^6 K corona (171 Å channel containing Fe IX and Fe X emission), and with *Yohkoh*-SXT. These images were selected because a full-disk image of a (nonhelium) transition region line near to solar minimum activity levels was available. Clearly, the EIT 171 Å image contains no detectable signature of transition region lines, even though a weak but potentially contaminating multiplet of O VI lies within the 171 Å EIT passband. By masking the EIT and *Yohkoh*-SXT images as shown to separate active regions and X-ray bright points from the quiet Sun, we find that the active Sun contributes ≈8% and 37% to the total irradiance in these EIT and *Yohkoh*-SXT images, respectively. Replacing the active region intensities with the average quiet Sun data in each image would reduce the irradiances by 6% and 31%, respectively. Thus, the *Yohkoh*-SXT irradiances are far more sensitive to the presence of small amounts of hotter active region plasma than are the EIT images, whose emission more accurately reflects plasma contributing to the softer spectra seen with *ROSAT*-PSPC and *SNOE*-SXP. Thus, it is potentially risky to use *Yohkoh*-SXT data to try to infer X-ray luminosities extending to the low energies sampled by the *ROSAT*-PSPC 0.1–2.4 keV passband. We believe that this problem is manifested by the fact that different authors have derived quite different values for the minimum solar luminosity using *Yohkoh*-SXT data: Schmitt (1997) determined $L^{\odot}_{\rm RASS} = 26.8$ ergs s^{-1}, but Acton (1996) found values of 25.5–26, and Orlando et al. (2001, their Fig. 6*a*) found $L^{\odot}_{\rm RASS} = 26$. The differing results depend on the modeling procedures used to convert *Yohkoh*-SXT to *ROSAT*-PSPC luminosities.

A second problem can be traced to the methods used by Orlando et al. (2001) to compute the emission measure distributions needed for their synthetic spectra. This issue had been recognized in earlier papers in their series (Orlando, Peres, & Reale 2000; Peres et al. 2000), but we believe that it leads to systematic errors under some important circumstances. From two filter measurements by *Yohkoh*-SXT, they derive for each pixel in each image a single temperature and a single value of the emission measure. A total "emission measure distribution" is derived for each image by adding up the total emission measures found in certain temperature bins (their Fig. 4, *right*). The resulting "distribution" then is taken as the input in a spectral calculation. Unfortunately, this can lead to a systematic bias in spectral simulation, because in principle one should first derive an emission measure distribution as a function of temperature for each pixel, and only afterward add the individual emission measure distributions to build up a valid composite for the whole Sun. The results will be correct *only* if the plasma observed in each pixel is truly isothermal. If material encompassing a wide range of temperatures falls along the line of sight, their monothermal analysis tends to pick a "mean" temperature—avoiding, in particular, any cooler coronal gas that is present (compare the EIT and *Yohkoh*-SXT images in Fig. 10)—therefore missing a critical part of the temperature structure required for an accurate calculation of the spectrum. The result is that the inactive part of their distribution of inferred X-ray luminosities is underestimated. Finally, independent measurements of irradiance made in the 1960s and 1970s show that the *Yohkoh*-SXT–based estimates of the amplitude of the solar cyclic variability in their quoted bands must be incorrect. For example, irradiances constructed from Tables 1 and 2 of Manson (1977) show that, when all radiation above 0.1 keV (123 Å) is included, the solar luminosity does not drop below $10^{26.8}$ ergs s^{-1}, within the quoted factor of ≈2 uncertainties. To drop to a value of 3×10^{25} ergs s^{-1}, one must include only the part of the spectrum above 0.4 keV.

In summary, we depart from the following assessment of Haisch & Schmitt (1996): "The solar coronal luminosity has been widely cited for years as ranging from 10^{27} ergs s^{-1} at solar minimum to 10^{28} ergs s^{-1} at solar maximum (excluding flares) (cf. Golub et al. 1982). It now appears that the inactive Sun may have a significantly lower L_x." Instead we believe that Golub and colleagues were nearer to the mark.

4.2. *The Sun in Comparison with the Stars*

As noted above, the sample of stars plotted in diagrams such as Figure 7 derived from all-sky survey data is biased by intrinsically brighter coronal sources, skewing the

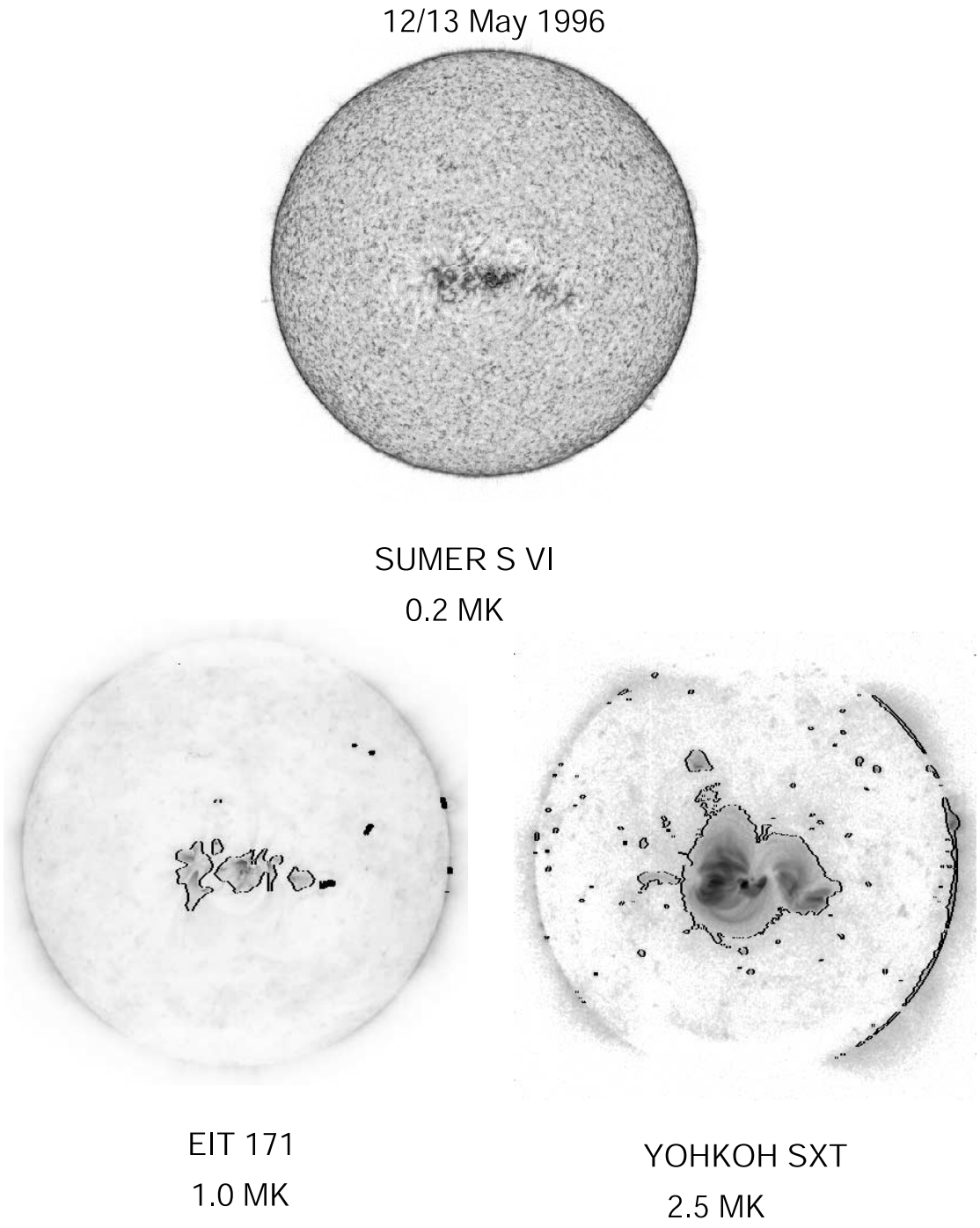

FIG. 10.—Full-disk images from the SUMER (S VI) and EIT (171 Å channel containing Fe IX, Fe X) on *SOHO* and *Yohkoh*-SXT for 1996 May 12/13. The EIT and *Yohkoh*-SXT images have color tables linear in the intensity, but the SUMER image's color table is not known (it was taken from http://www.linmpi.mpg.de/english/projekte/sumer). The active regions and bright points (demarcated within the contours) contribute ≈8% and 37% to the total irradiance in the EIT and *Yohkoh*-SXT images, respectively.

distributions toward higher luminosities. By supplementing RASS data with targeted observations, Schmitt (1997) constructed a volume-limited ($d < 13$ pc) sample of A, F, and G stars. The fit to his derived distribution function for G stars ($0.61 < B-V < 0.8$), taken from his Table 3, is shown as the smooth dot-dashed curve in Figure 7, except that we have moved his luminosities upward by 50% to bring his data approximately into consistency with our evaluation of the energy budget (see § 2.4 and Fig. 3). Note that Schmitt used equation (19) to convert his count rates to luminosities when hard photons were detected; otherwise, he used an HR-independent conversion factor of 6×10^{-12} ergs cm^{-2} count^{-1}. The difference between Schmitt's curve and the distribution derived from the data of Hünsch et al. (1998, 1999) is that it is volume limited, not flux limited. Within the quantifiable uncertainties, the comparison of the Sun's histogram with Schmitt's reveals the Sun to be a typical G-type star, which experiences fluctuations in its luminosity far smaller than the fluctuations seen between stars. The median solar luminosity is in good agreement with Schmitt's

volume-limited sample of G stars. Thus, our analysis essentially removes the systematic offset between the medians of the solar and stellar behavior noted by Schmitt, which indicated to him that the Sun is anomalously weak. Our extrapolated luminosity histograms move the median values downward, perhaps lending some support to Schmitt's claim, but this difference is far smaller than the width of Schmitt's distribution. In short, our conclusion that the Sun is quite typical differs from that of Schmitt (1997), essentially because he believed that the value of $L_X^{\odot}$ was, at solar maximum, only $\approx 2 \times 10^{27}$ ergs s^{-1}. Instead, it is probably closer to 6×10^{27} ergs s^{-1} (Figs. 6 and 7).

Finally, we draw attention to the dozen dwarf stars marked in Figures 7 and 8 whose measured X-ray properties make them interesting candidates as solar twins. There are also five or so subgiant stars of potential interest as indicators of the later evolution of the Sun's X-ray emission.

4.3. *Rotational and Cyclic Modulations*

We now turn to the question of why solar-like activity cycles or rotational modulation have not been widely reported in G-type stars. Several attempts (e.g., by Hempelmann, Schmitt, & Stepien 1996; Stern et al. 2003) have failed to find conclusive evidence for cyclic variability. Given the cyclic modulation of Ca II data seen in between 54% and 80% of FGK main-sequence stars (Baliunas et al. 1995; Saar & Brandenburg 1999) and the nonlinear relationship between stellar Ca II and X-ray emission, should not stellar cycles have been hinted at with *ROSAT*-PSPC? At least part of the answer may lie within Figure 7, which shows that the predicted solar peak-to-peak 0.1–2.4 keV amplitude lies between factors of 5 and 10, including variations due to rotation modulation. Thus, the amplitude of solar cyclic variations expected in the 0.1–2.4 keV passband might be substantially smaller than the order of magnitude or higher assumed by some authors (e.g., Hempelmann et al. 1996).

To investigate this issue, Figure 11 shows the computed variations of $L_{\rm RASS}$ as derived from the C IV regression. The peak-to-peak variation of $\log_{10} L_{\rm RASS}$ seen over the entire solar cycle sampled in the figure is $\approx$1.0. Breaking down the variations into long-term (>81 days) "cyclic" and short-term (<81 days) "rotational" components, the figure shows that long-term peak-to-peak variations are $\approx$0.8 dex, the rotational component contributing typically an rms variation of 0.06 dex. Given the 0.1–0.2 dex smaller variations computed using the F10.7 and *Yohkoh*-SXT extrapolations, we estimate that *the greater than 81 day "cyclic" component of the solar X-ray luminosity, as might have been observed by ROSAT-PSPC, varies only by a factor of 5–6 from solar minimum to maximum*. This result can help to explain why cyclic variations have not been seen conclusively in other stars.

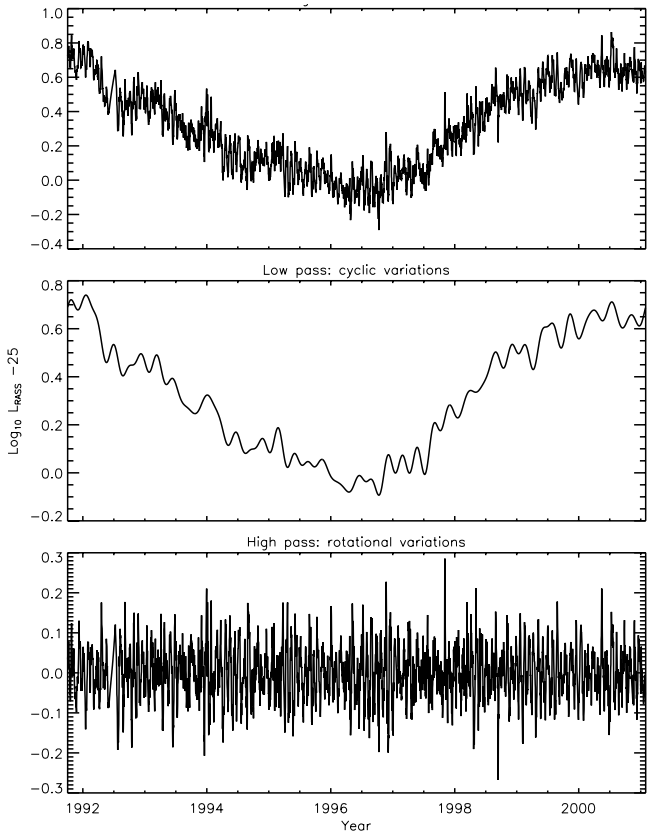

FIG. 11.—Expected variations of $\log_{10} L_{\rm RASS}$ as derived from regression of the *SNOE*-SXP currents with the C IV irradiances from SOLSTICE. *Top*: Unfiltered data. *Middle*: Low-pass Fourier filtered data set for which the maximum frequency corresponds to 1/81 days, or three solar rotations. *Bottom*: Complementary high-pass data set, showing mostly rotational modulation.

4.4. α *Cen A as a Solar Twin?*

As a case study of a star very similar to the Sun, in which to look for rotational modulation and cyclic variability, one star, α Cen A (G2 V), must be considered a prime candidate. It has been observed repeatedly with the *ROSAT* High Resolution Imager (HRI), in which it is sufficiently separated from the X-ray brighter K-type companion (α Cen B: K1 V) for an accurate flux measurement (Fig. 1*b* of Schmitt 1997). α Cen was observed by the HRI over the period 1995.6–1998.1, with extensive monitoring of the binary during two approximately month-long intervals in 1996. During the first of these, 1996.1–1996.2, both A and B were relatively constant with a flux ratio of $f_A/f_B \sim 0.35$, although one of the pointings in the middle of the series shows evidence for a factor of 2 X-ray enhancement—a "flare"—on the K star. In contrast, during the second period, 1996.6–1996.7, the K star showed a steady, systematic 40% decline from its previous X-ray level, but with several periods of transiently enhanced fluxes. The A/B flux ratio during this period was closer to 60%. Even α Cen A displayed a significant amount of systematic variation, also at the $\sim$40% level, perhaps due to rotational modulations. In the final, isolated HRI observation in 1998.1, α Cen A was close to its mean level of the full time series, but B had fallen substantially from its mean, down to that of A. Thus, in general, the X-ray flux of α Cen A is only half that of its cooler companion (as known since the *Einstein* era: see Schmitt 1997), but long- and short-term variability can change the ratio significantly.

The luminosity of α Cen A shown in Figure 5 was based on PSPC exposures in which the binary is not resolved. The apparent flux is comparable to the Sun under maximum conditions but is strictly an upper limit for α Cen A owing to the presence of the usually dominant companion's coronal emission. The HRI observations of α Cen A suggest an average $L_X \sim 1.5 \times 10^{27}$ ergs s^{-1}, with a $\sim\pm$30% variability over 1995–1998, near the bottom of the solar range. The corresponding surface fluxes would be comparatively even lower since α Cen A has a $\sim$50% larger surface area than the

Sun (e.g., Thévenin et al. 2002; also compare our Figs. 5 and 6). The ±30% variability observed is compatible with a random sampling of the solar-like rotational modulations seen in the bottom panel of Figure 11. Interestingly, the same figure suggests that the star's behavior is not compatible with solar-like cyclic variability unless α Cen A were near maximum or minimum activity levels during 1995–1998. Taken together, these findings suggest that α Cen A might be very similar to the Sun if it can be subsequently shown that 1995–1998 was a period of minimum activity for this star.

5. CONCLUSIONS

Our results can be summarized as follows:

1. Using *SNOE*-SXP data, we can estimate the behavior of the Sun as seen in the 0.1–2.4 keV ("RASS") passband of *ROSAT*-PSPC to within ±50%, not counting sources of systematic uncertainty discussed in the Appendix.

2. We find that the Sun's 0.1–2.4 keV luminosity lies between $10^{27.1}$ and $10^{27.75}$ (measured over the time span of the *SNOE*-SXP data) and between $10^{26.8}$ and $10^{27.9}$ (extrapolated over a full activity cycle). This behavior places it among the least active late-F and G stars in the brightness-limited samples of Hünsch et al. (1998, 1999).

3. In comparison with a volume-limited ($d < 13$ pc) sample of G stars from Schmitt (1997), the Sun's luminosities lie very close to the median stellar behavior but exhibit only small temporal deviations compared to the overall spread of X-ray luminosities in the stellar sample.

4. We predict (Figs. 4 and 11) that a solar-like star should show factors of typically 1.5 peak-to-peak variations in the RASS passband simply because of rotational modulations of active regions.

5. The solar cyclic variations are less easy to predict, owing in part to the fact that *SNOE* missed the solar minimum of 1996–1997. Extrapolations and earlier solar observations indicate solar cyclic variations are 0.7–0.8 in $\log_{10} L_{\rm RASS}$, or a ratio of 5–6 in the maximum to minimum values. Superposed on this is the smaller amplitude rotational modulation.

6. Repeated *ROSAT* observations of α Cen A show that it appears to behave like the Sun during activity-minimum conditions. It remains to be seen how alike the activity cycles of these stars really are.

We are grateful to Scott Bailey for assistance with the *SNOE*-SXP data, to Tom Woods for providing the SOLSTICE data, to Scott McIntosh for allowing us to use his IDL genetic algorithm, and to Tim Brown for a careful reading of the manuscript. P. G. J. thanks Jürgen Schmitt for reading the manuscript and for useful discussions. We thank L. W. Acton for processing and providing the *Yohkoh*-SXT data. G. Peres made several valuable suggestions for improving the manuscript.

APPENDIX

SOURCES OF SYSTEMATIC ERROR

As well as the known sources of error discussed in the main text, our analysis hinges on the accuracy with which the synthetic spectra match real data over extended energy ranges (see Fig. 1 and eqs. [9] and [12]). There is no way to judge the magnitude of uncertainties that might arise from such systematic errors in our calculations. However, we offer the following justification in support of the calculations done. The CHIANTI package was chosen because of its overall success at accounting for solar coronal spectra at longer wavelengths than are important here (Young, Landi, & Thomas 1998; Landi, Feldman, & Dere 2002) and because of the recent inclusion of atomic data for abundant H-like and He-like ions that extend the completeness of computed spectra down to the wavelength limit of a few Å, the lowest wavelengths at which the instruments are sensitive. To our knowledge, no quantitative comparison between computed and observed solar or stellar spectra throughout the entire *ROSAT*-PSPC and *SNOE*-SXP wavelength ranges exists. Using early atomic and solar data, good agreement has, however, been found for important transitions of certain H- and He-like ions (Gabriel & Jordan 1971). Furthermore, comparison of early measurements (e.g., Tables 1 and 2 of Manson 1977; Table 2 of Kreplin et al. 1977) with the CHIANTI calculations shows that the CHIANTI line list contains all of the strong lines of importance to the irradiance. Dere et al. (2001) have shown that there remain some gaps in the atomic data, however. Such gaps correspond to weak transitions in abundant ions or stronger transitions in ions of elements with low abundances. In either case they contribute little to the total X-ray emission over relatively broad bands.

The level of agreement exhibited in Figure 2, yielding rms values of ±14% in the residuals of the fits given by equation (17), is typical for the RASS passband in two more abundance sets given by the CHIANTI project's database. Photospheric abundances were also taken from Anders & Grevesse (1989), updated using data from Grevesse & Noels (1993), Grevesse, Noels, & Sauval (1992), and Young et al. (1997). "Coronal" abundances were examined using data from Meyer (1985) as well as from Feldman et al. (1992b). The photospheric abundance sets used were very similar. The coronal abundance sets differ substantially according to the first ionization potential (FIP) of a given element. In Meyer's work, the abundances of high-FIP elements are factors of 3 or so lower than their photospheric values; in Feldman's work, the low-FIP elemental abundances are a similar factor higher than photospheric values. The main influence of varying the abundances is to alter the shape of the mean photon flux densities $\langle F^i \rangle (T_e)$ and the coefficients c_{ij} in equation (16). The luminosities and energy flux densities remain almost independent of the abundances used.

It is important to note that the coefficients c_{ij} in equation (17) were determined using the *same* set of abundances for *both* the Sun *and* the stars. If the Sun conspired to have coronal abundances that were systematically different from essentially all other stars, then additional systematic errors would be introduced through the erroneous prediction of the Sun's *ROSAT*-PSPC count rates. To our knowledge, there is no reason to believe that the Sun is in such an anomalous state.

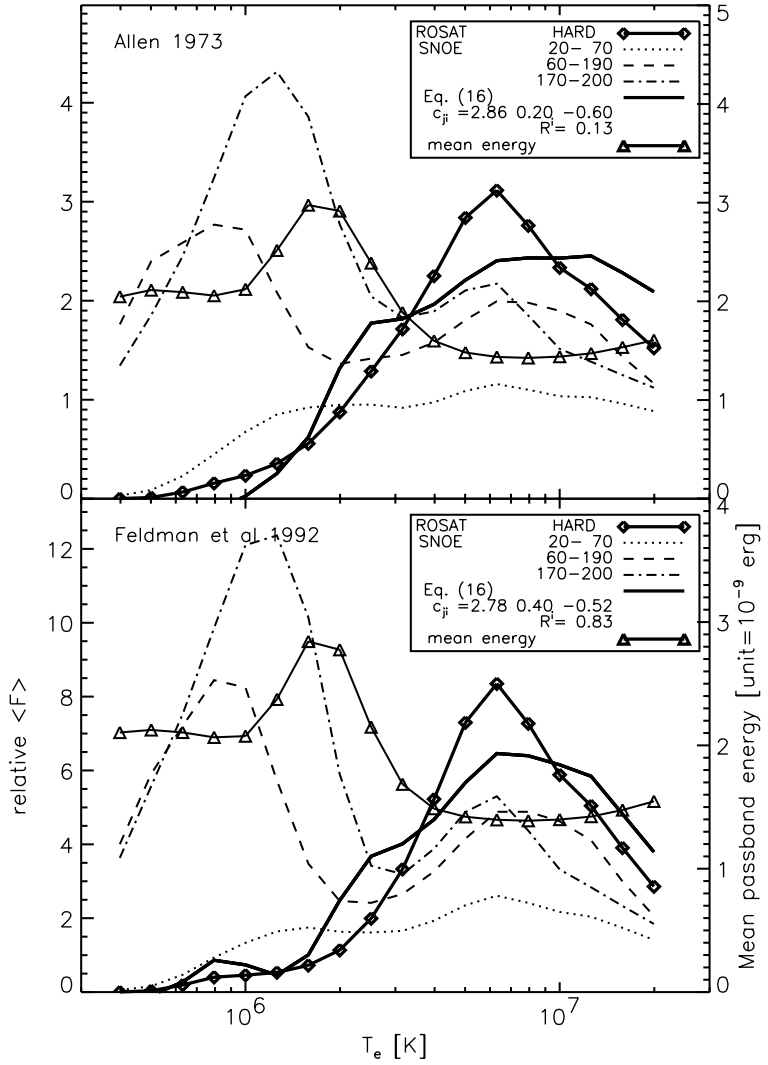

FIG. 12.—Mean flux densities for the hard *ROSAT*-PSPC passband (0.52-2 keV), plotted as in Fig. 2

A problem arises when attempting to convert *SNOE*-SXP data into the *ROSAT*-PSPC *H* passband. Figure 12 shows the fits for the *H* passband, similar to those shown in Figure 2. Judging from these figures, one might expect to be able to predict the *H* bandpass behavior quite accurately, from the *SNOE*-SXP measurements. However, as mentioned in the main text, there is an additional problem with the *H* passband. The count rates in this channel are particularly sensitive to uncertainties in the poorly determined *SNOE*-SXP effective areas at high energies. To test this, we computed count rates as seen in the various *ROSAT*-PSPC bandpasses, using equation (18) as in the main text, but in two " perturbed " cases where the high-energy parts of the effective areas (i.e., those beyond the nominal bandpasses listed in the text) were multiplied by factors of 0.5 and 2. The resulting count rates in the RASS and *S* bandpasses both differed from the unperturbed calculation by ≈30%. The count rates in the *H* bandpass differed, however, by factors of 2. The actual uncertainties in the high-energy parts of the effective areas are not known, so we err on the side of caution and do not trust the count rates for the *H* bandpass. This is supported by the fact that using equation (18) for the *H* channel yields hardness ratios HR near −0.16, whereas solar-type stars have measured values much closer to −1.

Finally, for each abundance set, similar calculations were done for a variety of electron pressures. The differences between the mean flux densities computed at electron pressures of 10^{14} and 10^{16} cm^{-3} K for the three *SNOE*-SXP channels and their sum are at most a few percent, much smaller than the differences between the summed *SNOE* mean flux densities and those of the *ROSAT*-PSPC. These differences therefore are negligible in our analysis.

REFERENCES

Acton, L. W. 1996, in ASP Conf. Ser. 109, Cool Stars, Stellar Systems, and the Sun: Ninth Cambridge Workshop , ed. R. Pallavicini & A. K. Dupree (San Francisco: ASP), 45
Allen, C. W. 1973, Astrophysical Quantities (3d ed.; London: Athlone)
Anders, E., & Grevesse, N. 1989, Geochim. Cosmochim. Acta, 53, 197
Arenou, F., Lindegren, L., Froeschle, M., Gomez, A. E., Turon, C., Perryman, M. A. C., & Wielen, R. 1995, A&A, 304, 52
Ayres, T. R. 1997, J. Geophys. Res., 102, 1641
Ayres, T. R., Marstad, N., & Linsky, J. L. 1981, ApJ, 247, 545
Bailey, S. M., Woods, T. N., Barth, C. A., Solomon, S. C., Canfield, L. R., & Korde, R. 2000, J. Geophys. Res., 105, 27179
Baliunas, S. L., et al. 1995, ApJ, 438, 269
Barnes, T. G., Evans, S., & Moffett, T. J. 1978, MNRAS, 183, 285
Briel, U. G., & Pfeffermann, E. 1995, Proc. SPIE, 2518, 120

Charbonneau, P., & Knapp, B. 1995, A User's Guide to PIKAIA 1.0 (Technical Rep. NCAR/TN-418+IA, National Center for Atmospheric Research)
Dere, K. P., Landi, E., Young, P. R., & Del Zanna, G. 2001, ApJS, 134, 331
Feldman, U. 1998, Space Sci. Rev., 85, 227
Feldman, U., Laming, J. M., Mandelbaum, P., Goldstein, W. H., & Osterheld, A. 1992a, ApJ, 398, 692
Feldman, U., Mandelbaum, P., Seely, J. L., Doschek, G. A., & Gursky, H. 1992b, ApJS, 81, 387
Fleming, T. A., Molendi, S., Maccacaro, T., & Wolter, A. 1995, ApJS, 99, 701
Gabriel, A. H., & Jordan, C. 1971, in Case Studies in Atomic Collision Physics, ed. E. W. McDaniel & M. R. C. McDowell (Amsterdam: North-Holland), 210
Golub, L., Harnden, F. R., Pallavicini, R., Rosner, R., & Vaiana, G. S. 1982, ApJ, 253, 242
Gray, D. F. 1992, PASP, 104, 1035
Grevesse, N., & Noels, A. 1993, Phys. Scr., T47, 133
Grevesse, N., Noels, A., & Sauval, A. 1992, in Coronal Streamers, Coronal Loops, and Coronal and Solar Wind Composition, ed. C. Mattock (ESA SP-348; Paris: ESA), 305
Gustafsson, B. 1998, Space Sci. Rev., 85, 419
Haisch, B., & Schmitt, J. H. M. M. 1996, PASP, 108, 113
Hara, H., Tsuneta, S., Acton, L. W., Bruner, M. E., Lemen, J. R., & Ogawara, Y. 1994, PASJ, 46, 493
Hempelmann, A., Schmitt, J. H. M. M., & Stepien, K. 1996, A&A, 305, 284
Hünsch, M., Schmitt, J. H. M. M., Sterzik, M. F., & Voges, W. 1999, A&AS, 135, 319
Hünsch, M., Schmitt, J. H. M. M., & Voges, W. 1998, A&AS, 132, 155
Kreplin, R. W., Dere, K. P., Horan, D. M., & Meekins, J. F. 1977, in The Solar Output and Its Variations, ed. O. R. White (Boulder: Colorado Assoc. Univ. Press), 287
Landi, E., Feldman, U., & Dere, K. P. 2002, ApJS, 139, 281
Manson, J. E. 1977, in The Solar Output and Its Variations, ed. O. R. White (Boulder: Colorado Assoc. Univ. Press), 261
Meyer, J.-P. 1985, ApJS, 57, 173
Orlando, S., Peres, G., & Reale, F. 2000, ApJ, 528, 524
———. 2001, ApJ, 560, 499
Pallavicini, R., Golub, L., Rosner, R., & Vaiana, G. 1981, in Second Cambridge Workshop on Cool Stars, Stellar Systems, and the Sun, Vol. 2, ed. M. S. Giampapa & L. Golub (SAO Special Rep. 392; Cambridge: SAO), 77
Peres, G., Orlando, S., Reale, F., Rosner, R., & Hudson, H. 2000, ApJ, 528, 537
Raymond, J. C., & Smith, B. W. 1977, ApJS, 35, 419
Rutten, R. G. M., & Schrijver, C. J. 1987, A&A, 177, 155
Rutten, R. G. M., Schrijver, C. J., Lemmens, A. F. P., & Zwaan, C. 1991, A&A, 252, 203
Saar, S. H., & Brandenburg, A. 1999, ApJ, 524, 295
Schmitt, J. H. M. M. 1997, A&A, 318, 215
Schmitt, J. H. M. M., Fleming, T. A., & Giampapa, M. S. 1995, ApJ, 450, 392
Schrijver, C. J. 1983, A&A, 127, 289
———. 1987, A&A, 180, 241
Solomon, S. C., Bailey, S. M., & Woods, T. N. 2001, Geophys. Res. Lett., 28, 2149
Stern, R. A., Alexander, D., & Acton, L. W. 2003, in ASP Conf. Ser., Cool Stars, Stellar Systems, and the Sun: Twelfth Cambridge Workshop (San Francisco: ASP), in press
Taylor, B. J. 1984, ApJS, 54, 167
Thévenin, F., Provost, J., Morel, P., Berthomieu, G., Bouchy, F., & Carrier, F. 2002, A&A, 392, L9
Vaiana, G. S., & Rosner, R. 1978, ARA&A, 16, 393
Walker, A. B. C. 1977, in The Solar Output and Its Variations, ed. O. R. White (Boulder: Colorado Assoc. Univ. Press), 279
Young, P. R., Landi, E., & Thomas, R. J. 1998, A&A, 329, 291
Young, P. R., Mason, H. E., Keenan, F. P., & Widing, K. G. 1997, A&A, 323, 243